JOURNAL OF MATERIALS SCIENCE 25 (1990) 4194–4202

The bonding mechanism of aramid fibres to epoxy matrices

Part II *An experimental investigation*

J. KALANTAR, L. T. DRZAL
Composite Materials and Structures Center, Michigan State University, East Lansing, Michigan 48824-1326, USA

In this study attempts are made to develop a basic understanding of the interfacial interactions resulting from the combination of aramid fibres with epoxy matrices in composite materials. The interfacial interactions examined are mechanical stresses due to fibre-matrix thermal strains and Poisson's ratio mismatch, covalent chemical bonding, fibre-matrix wetting, and effects of physicochemical weak boundary layers. Both aramid and carbon fibres have been examined to assess the interfacial interactions by comparing the behaviour of these two fibres in the same matrices. The results indicate that the adhesion of aramid fibres to epoxy matrices lack both the mechanical and the chemical interactions present at the carbon–epoxy interface. Aramid fibres exhibit an interfacial shear strength much lower than the expected theoretical value. Direct observation of the aramid–epoxy interface by transmission electron microscopy shows fibrillar separations within the fibre surface, which may be the limiting factor in achieving greater interfacial adhesion.

1. Introduction

Aramid fibres have a unique combination of stiffness, high strength, and low density that rivals the properties of inorganic reinforcing fibres such as glass and carbon fibres. Advanced composites made of aramid fibres have excellent axial properties compared to inorganic fibres, but their off-axis properties are less than the optimum for some applications. The off-axis properties of fibre-reinforced composites are generally controlled by the level of fibre–matrix adhesion. The interface between aramid fibres and epoxy matrices does not attain the level of adhesion reached by other reinforcing fibres. A prerequisite for improving aramid composite performance is a basic understanding of the mechanisms that affect the fibre–matrix adhesion.

This study has been undertaken to examine the interactions between aramid fibres and epoxy matrices. Effects of mechanical and chemical interactions at the fibre–matrix interface are examined and experimental results are compared with results of a theoretical model. A direct observation of the aramid–epoxy interface is carried out by microtoming the single-fibre samples and examining them by transmission electron microscopy.

Based on previously reported work, the most probable mechanisms affecting fibre–matrix adhesion are mechanical stresses, chemical interactions, and physicochemical weak boundary layers. Mechanical stresses are the result of thermal shrinkage and the Poisson's ratio difference between fibre and matrix. Chemical interactions involve covalent bonding and fibre–matrix wetting. Weak boundary layers are formed by surface layers with lower cohesive or adhesive properties than their bulk counterparts resulting in a reduction in efficiency of load transfer at the interface.

The approach of this study is to separate and qualitatively analyse the mechanical and chemical interactions of the interface. The manipulation of the interface was achieved by application of controlled boundary layers and variation of the resin curing temperatures. Gold and silicone coating of the fibres were two types of surface treatments examined that introduce physicochemically distinct boundary layers. Both coatings effectively eliminated all the covalent bonds that might be present at the fibre–matrix interface, and also modified the thermodynamics of the fibre surface. Gold coating produces an inert, yet thermodynamically wettable fibre surface. Silicone coating produces an inert, but non-wettable fibre surface.

Characterization of interfacial shear strength was obtained by a critical length measurement technique. For a system consisting of a fibre fragment surrounded by an unbounded matrix, a relation between critical length (l_c) and interfacial shear strength ($\bar{\tau}_{exp}$) was first demonstrated by Kelly and Tyson [1]

$$\bar{\tau}_{exp} = \frac{\sigma_{uf}}{2}\left(\frac{d}{l_c}\right) \quad (1)$$

where σ_{uf} is the fibre tensile strength (MPa) and d is the fibre diameter (μm). In this equation the l_c, the critical length (μm) is the final fragment length. The equation is derived by a force balance and provides a good characterization of the shear strength of the interface.

An analytical model of the three-dimensional stress

0022–2461/90 $03.00 + .12

distribution around an isolated fibre fragment proposed by Whitney *et al.* [2] was used to calculate the maximum theoretical stresses. The theoretical average interfacial shear ($\bar{\tau}_{theo}$) (MPa) and normal stresses ($\bar{\sigma}_{r,theo}$, theoretical average interfacial radial stresses (MPa)) were calculated from constituent properties and compared with experimental values. The model is described briefly in the appendix.

2. Experimental details

Aramid fibres used in this study were Kevlar 49 supplied by E. I. du Pont. To eliminate possible interferences by fibre sizing, the fibres were repeatedly washed in absolute ethanol. Carbon fibres used in this study were AS-4 fibres, supplied by Hercules.

The matrix was an amine cured epoxy. The epoxy resin was DER331 which is a diglycidyl ether of bisphenol A (DGEBA) epoxy (Dow Chemical). The curing agents were diethylenetriamine (DETA) (Aldrich) and a mixture of two curing agents metaphenylenediamine (MPDA) (Aldrich) and diethyltoluenediamine (DETDA) (Ethyl Corporation). The DER331–DETA system and the DER331–MPDA–DETDA system were formulated at the stoichiometric ratios.

Samples used for the critical length measurements were cured resin dogbones with single fibres embedded along their centres. The technique and the sample preparation have been described by Drzal *et al.* [3]. For the carbon fibres with brittle fractures, the critical lengths were directly measured using a motorized stage with a displacement readout. For the aramid fibres, the failure occurs by fibrillation over a long distance and exact fracture lengths could not be determined. The average critical lengths of the aramid fibres were obtained by counting the number of failed regions within a 22 mm fibre length.

Four curing temperatures (ambient, 75° C, 125° C, and 175° C) were selected for this study. For the ambient and 75° C curing temperatures, the DETA curing agent was used. DETA is a very reactive amine curing agent, however, at low curing temperatures the system was too brittle for critical length testing. Subsequent post-curing of the DETA systems was required to increase their fracture strain. The post-curing time and temperatures were determined by the glass transitions, T_g (° C), of the matrix. During the post-cure, the oven temperature was maintained below the T_g of the matrix to avoid building up thermal stresses. At each post-curing temperature, initially the T_g was only a few degrees above the oven temperature. After a certain time the glass transition temperature increased and the oven temperature was raised.

Thermal expansion and glass transition of the matrix were measured with a du Pont thermal mechanical analyser (TMA model 943). The elastic modulus of the epoxy matrices at the ambient temperatures were measured with a du Pont dynamic mechanical analyser (DMA model 983), run isothermally at 1 Hz fixed frequency for 5 minutes.

3. Results and discussion

3.1. Thermal stresses

Cooling of a composite from oven temperature to ambient temperature results in thermal shrinkage of the fibre and the matrix. To examine the effects of thermal stresses on fibre–matrix adhesion, samples of epoxy dogbones were cured at ambient (nominally 25° C), 75° C, 125° C, and 175° C curing temperatures. Fig. 1 illustrates the TMA results for the thermal shrinkage of these epoxy systems. The epoxy system cured at the room temperature was subjected to an extensive post-curing that resulted in ~0.12% post-curing shrinkage.

Fig. 2 presents the experimental interfacial shear strength ($\bar{\tau}_{exp}$) of untreated aramid–epoxy and carbon–epoxy samples cured at the four curing temperatures. Over the curing temperature range, the aramid samples exhibit 3.5 to 5 times lower $\bar{\tau}_{exp}$ than the carbon samples. The carbon samples exhibit increasing fibre–matrix adhesion with increasing curing temperatures, but for the examined curing conditions the aramid samples are unaffected by the curing temperatures.

The overall radial thermal stress at the fibre–matrix interface is due to two opposing mechanisms. One is radial thermal shrinkage of fibre and matrix and the other is radial expansion of fibre due to its axial contraction. During cool down from oven temperature to ambient conditions the isotropic matrix shrinks uniformly, but the orthotropic fibre tends to axially expand and radially shrink. For the single fibre specimen, the thermal shrinkage of the matrix actually compresses the fibre in its axial direction since the single fibre can not resist the large matrix deformations.

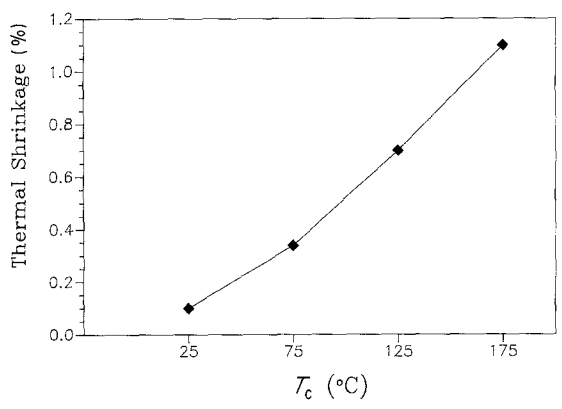

Figure 1 Plot of % thermal shrinkage of the epoxy matrices for different curing temperatures.

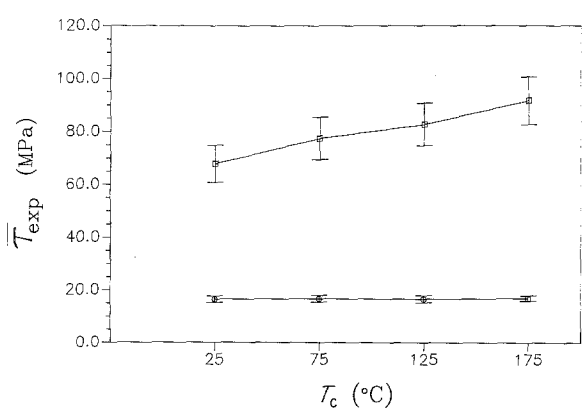

Figure 2 Plot of experimental interfacial strength of untreated carbon (□) and aramid (○) fibres for different curing temperatures.

TABLE I Thermal expansion coefficients and Poisson's ratio of Kevlar 49, AS-4, and epoxy

Property	Reference	Kevlar 49	AS-4	Epoxy
ν	[2]	0.35	0.25	0.35
α_1 (p.p.m. $°C^{-1}$)	[2, 4]	−5.72	−1.1	70
α_2 (p.p.m. $°C^{-1}$)	[2, 4]	65	8.5	70

α_1 and α_2 are the axial and radial coefficients of thermal expansion (p.p.m. $°C^{-1}$), respectively.

The fibre axial contraction in turn results in fibre radial expansion due to its Poisson's ratio. The other effect is radial shrinkage of the fibre and the matrix due to temperature cool down. Therefore, the net interfacial radial thermal stress is due to overall effect of the two opposing thermal strain mechanisms. Table I compares the thermal expansion properties and the Poisson's ratio of the fibres and the matrix.

For the carbon fibre the difference between its radial thermal shrinkage and the epoxy thermal shrinkage create radial thermal stresses. However, for the aramid fibres the close match between the radial thermal shrinkage of the fibre and the epoxy matrix results in low thermal stress contribution from the radial shrinkage. Penn *et al.* [5] have suggested the lower level of thermal stresses in aramid composites as an important reason for their relatively weaker interfacial adhesion.

For both aramid and carbon fibres the radial expansion due to the fibre axial compression should contribute to the radial thermal stress. However, for the examined curing conditions aramid samples show no temperature trends (Fig. 2) suggesting a failure mechanism unaffected by these curing temperatures. The effects of the thermal stresses are discussed further in the stress model section.

3.2. Poisson's ratio mismatch

The Poisson's ratio mismatch between the fibre and the matrix can result in contraction of the matrix around the fibre when a load is applied to the composite. For the fibre with a lower Poisson's ratio than matrix, on application of an axial tension to the composite the matrix shrinks radially to a greater extent than the fibre, resulting in a radial compressive load. Fig. 3 compares the interfacial shear strength of gold coated, silicone coated, and untreated aramid and carbon samples made with the room temperature cured epoxy. The carbon samples generally exhibit higher $\bar{\tau}_{exp}$ values than the aramid samples for both coated and untreated fibres. The room cured matrix has very low thermal stresses and the coated fibres have no covalent chemical bonding at their interface. For the coated fibres the main interfacial interactions are due to the Poisson's ratio mismatch, fibre–matrix wetting, and the coating boundary layers. Both the gold coated and the silicone coated carbon samples have $\bar{\tau}_{exp}$ values two and half times the values of corresponding aramid samples. Since the coated aramid and carbon fibres have the same surface wetting and coating boundary layer, the higher adhesion of the coated carbon fibres shows the effect of Poisson's ratio mismatch. Drzal *et al.* [6], in comparing the interfacial behaviour of aramid and carbon composites, have suggested that both the lower thermal and Poisson's ratio mismatch of aramid–epoxy are adversely affecting their interfacial adhesion.

3.3. Chemical bonding

Coating the fibres by an inert material such as gold eliminates all possible covalent bonds at the fibre–matrix interface, while maintaining a thermodynamically wettable surface. Fig. 4 demonstrates the affects of the two different epoxy systems on the interfacial shear strengths of gold coated and untreated fibres. The untreated carbon samples exhibit a greater interfacial shear strength for both the 75° C cured DETA system and 125° C cured MPDA–DETDA system than the corresponding gold coated carbon samples. For the aramid fibre all samples exhibit similar adhesion at both temperatures with a small adhesion reduction for the gold coated fibres.

The observation suggests that the reactivity of the resin can affect the carbon–epoxy adhesion, but not the aramid–epoxy adhesion. For the gold coated aramid fibres the small adhesion reduction can be attributed to the effect of the gold weak boundary layer. Garton [7] has the examined aramid–epoxy interface with FT–IR and has not observed any significant alteration of the epoxy crosslinking by the aramid surface. For the carbon fibres, Drzal *et al.* [8] have shown evidence of weak chemical interactions that could be due to reaction of epoxy groups with hydroxyl and carboxyl surface groups [9].

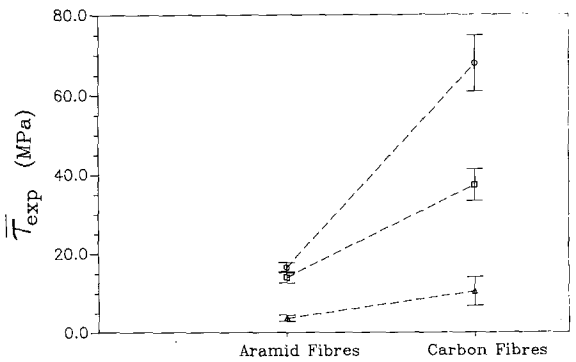

Figure 3 Plot of experimental interfacial shear strength of untreated (○) gold coated, (□) and silicone coated (△) carbon and aramid fibres for the room cured epoxy matrix.

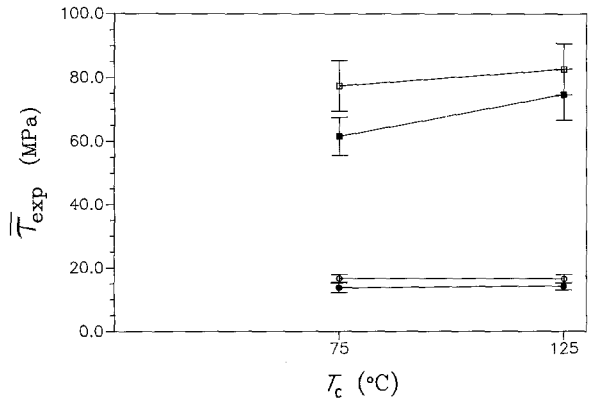

Figure 4 Plot of experimental interfacial shear strength of untreated (□) and gold coated (■) carbon and untreated (○) and gold coated (●) aramid fibres for 75 and 125° C curing temperatures.

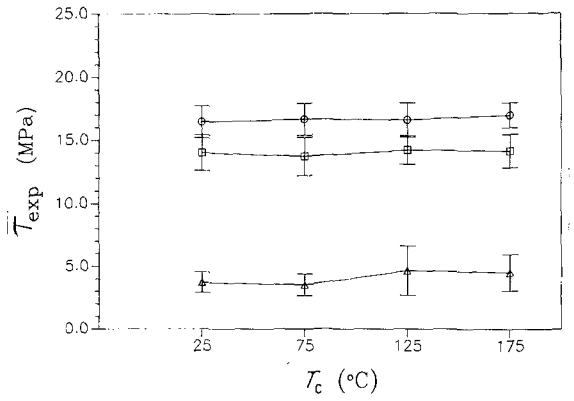

Figure 5 Plot of experimental interfacial shear strength of untreated (○) gold coated (□), and silicone coated (△) aramid fibres for different curing temperatures.

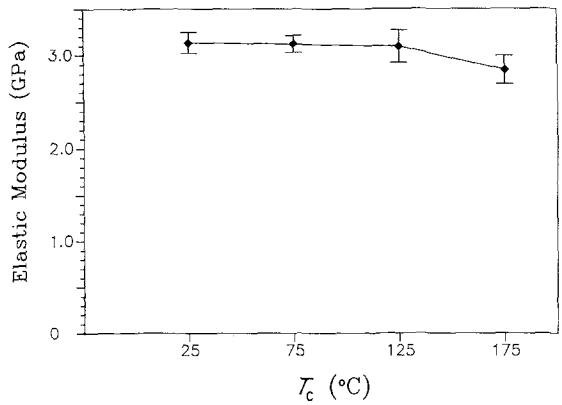

Figure 6 Plot of elastic modulus of the epoxy matrices for different curing temperatures.

3.4. Fibre wetting

Good wetting of the fibre by the liquid resin increases molecular interactions at the interface, which in turn enhances the load transfer to the fibre. Fig. 5 compares the experimental interfacial shear strength (MPa), $\bar{\tau}_{exp}$, values of the coated and untreated aramid fibres. Gold coated fibres give a $\sim 15\%$ reduction in $\bar{\tau}_{exp}$, while silicone coated fibres produce $\sim 75\%$ reduction. The metallic gold has a high surface tension, but the silicone is a mold release agent with very poor wetting properties. The drastic reduction of the silicone coated samples shows the importance of achieving thermodynamic wetting as a precondition for a good adhesion.

Works by Penn *et al.* [5] and Li *et al.* [10] have determined that the surface energies of carbon and aramid fibres are similar. Wesson *et al.* [11] have shown that the surface energies of aramid fibres and liquid DGEBA resin are also similar. From these results, both carbon and aramid fibres are expected to have similar good wetting with liquid epoxies.

3.5. Three-dimensional stress model

The experimental values of the interfacial shear strength have been determined by Equation 1, however, effects of the thermal stresses and Poisson's ratio mismatch are not explicitly present in this equation. A three-dimensional stress model proposed by Whitney *et al.* [2] was examined to acquire additional insights to the interfacial interactions. The material properties for fibres are presented in the Tables I and II. The ambient matrix elastic moduli have been determined by DMA and are plotted in Fig. 6. The matrix thermal expansions are given in the Fig. 1.

Whitney's model permits the evaluation of all stress and displacement components. Fig. 7 compares the experimental interfacial shear strength ($\bar{\tau}_{exp}$) and the theoretical average interfacial shear stress (MPa) ($\bar{\tau}_{theo}$). The experimental and the theoretical results for the carbon samples show good relation agreement with slight differences. The results for the aramid fibre, however, do not agree either in general trend or absolute values of stress. For both fibres, the theoretical results suggest that interfacial shear strength increases with increasing curing temperatures, although to a greater extent for the carbon fibres than for the aramid fibres. The model predicts good interfacial shear strength for both types of fibres.

The failure of the Whitney's model to reasonably predict the interfacial shear strength of the aramid fibres, suggests that a disparity exists between the model's assumptions and the physical events. The temperature independence of the theoretical critical length equation Equation (A8) is not expected to introduce severe errors to the aramid results because of the discussed similarities in the aramid and the epoxy thermal properties. The model assumes linear elastic fibre fragment and matrix deformations, however, the aramid fibres fail by internal axial cracking. Optical micrographs of aramid and carbon fibre fragments under bright-field and cross-polarized illumination are shown in Fig. 8. The aramid fibre shows long axial cracks and diffuse stress patterns indicating non-uniform bonding. Aramid fibre properties such as modulus, Poisson's ratio, and thermal strains may depart from linear elastic behaviour under these conditions of fibre axial fracture. Internal fibril slippage is

TABLE II Material properties of Kevlar 49 and AS-4 fibres

Property	Reference	Kevlar 49	AS-4
E_{1f} (GPa)	[6]	119	231
E_{2f} (GPa)	[12, 2]	0.77	21
G_{2f} (GPa)	[12, 2]	1.8	8.3
σ_{uf} (GPa)	[6]	3.31	5.86
ε_{uf} (%)	[6]	2.5	1.4

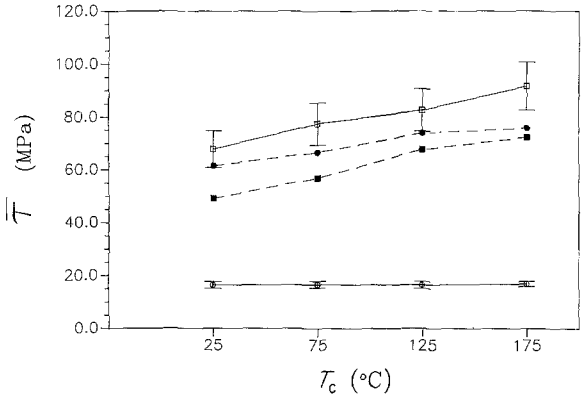

Figure 7 Plot of experimental and theoretical interfacial shear strength for aramid and carbon fibres for different curing temperatures. (○ experimental aramid, □ experimental carbon, ● theoretical aramid, ■ theoretical carbon).

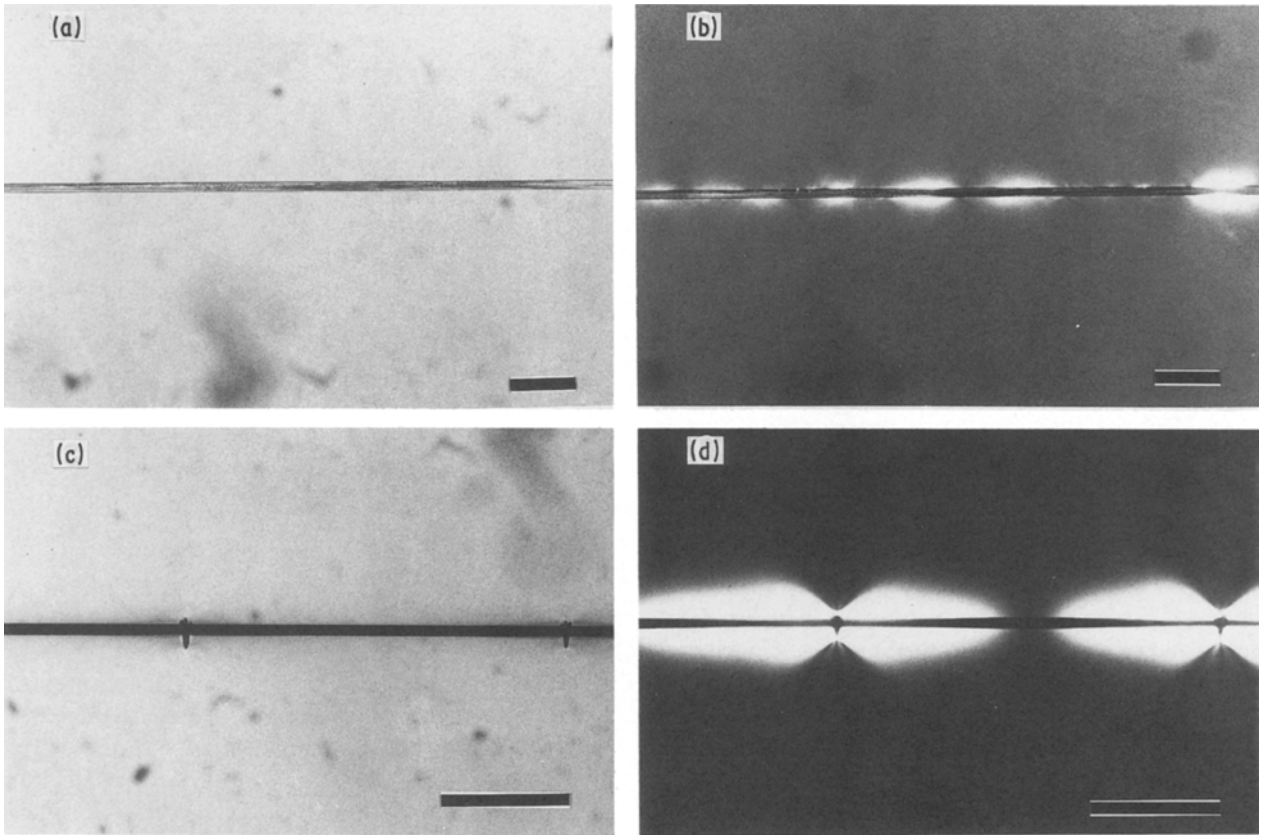

Figure 8 Optical micrographs of fibre fragments at their critical lengths. (a) Kevlar 49 under bright-field light. (b) Kevlar 49 under cross-polarized light. (c) AS-4 under bright-field light. (d) AS-4 under cross-polarized light. bar = 100 μm.

also possible, which violates the perfect bonding assumption of the model.

Interfacial radial stress is due to both thermal stresses and the Poisson's ratio mismatch. Since the fibre and the matrix are radially in series, the radial stress should be fully transferred across the interface. Therefore, the interfacial radial stress is expected to be less dependent on the extent of fibre–matrix bonding than other stresses. Fig. 9 compares the theoretical average radial stresses for both the aramid and the carbon samples. The carbon fibre samples show three to five times higher $\bar{\sigma}_{r,theo}$ values than the aramid samples. The higher $\bar{\sigma}_{r,theo}$ values of the carbon system can be attributed to both its higher thermal stresses and Poisson's ratio mismatch.

The temperature trends predicted for the aramid

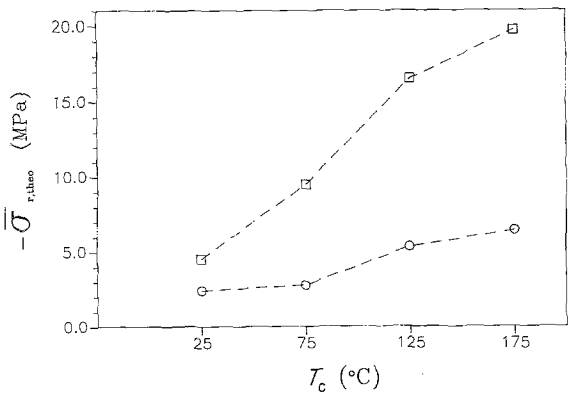

Figure 9 Plot of theoretical average interfacial shear stress for aramid (○) and carbon (□) fibres for different curing temperatures.

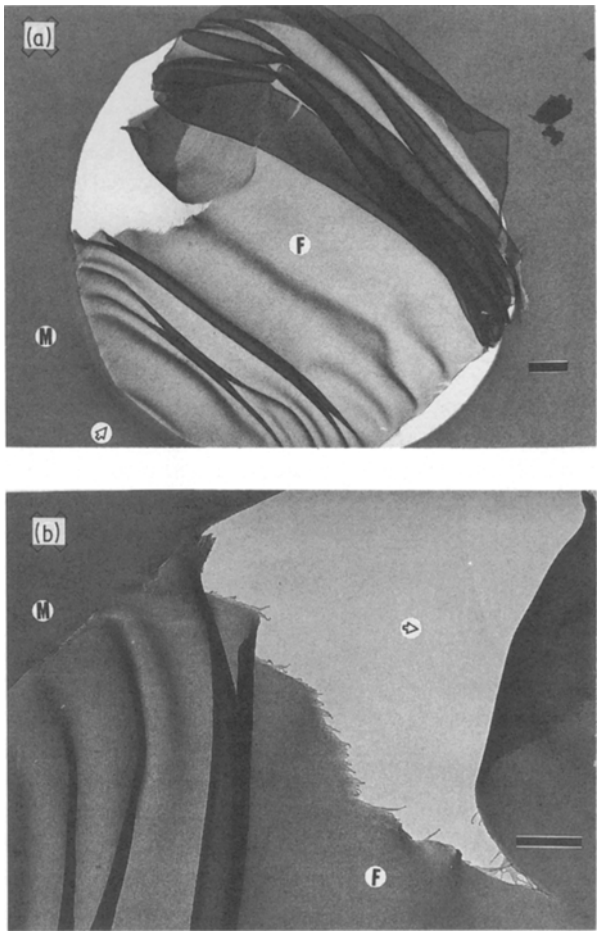

Figure 10 TEM micrograph of Kevlar in a room-cured epoxy system. The section is cut along the fibre radial direction. (a) bar = 1 μm, (b) bar = 500 nm.

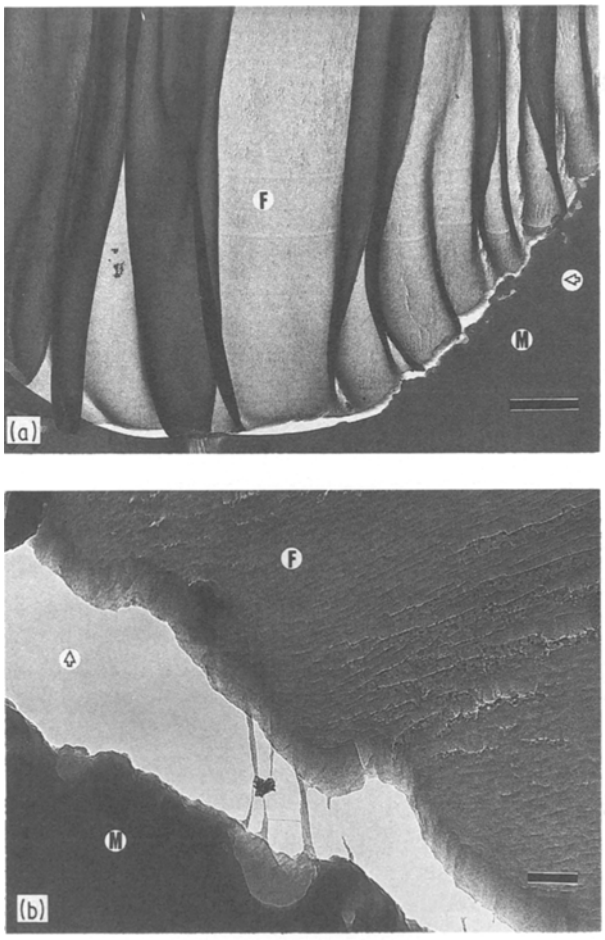

Figure 11 TEM micrographs of a surface damaged Kevlar 49 in a 175° C cured epoxy system. The section is cut along the fibre radial direction and stained with OsO_4. (a) bar = 1 μm, (b) bar = 100 nm.

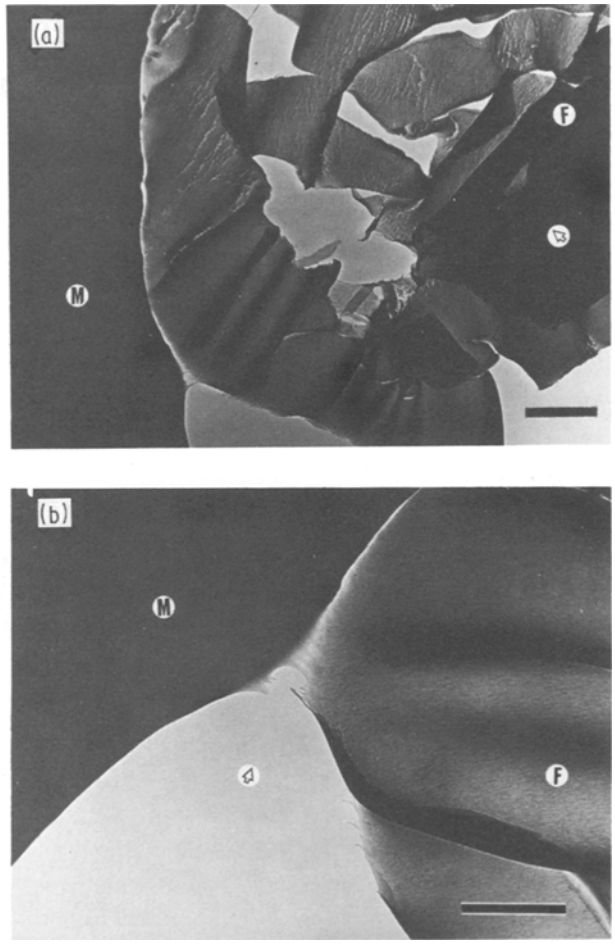

Figure 12 TEM micrographs of a shear damaged Kevlar 49 in a 75° C cured epoxy system. The section is cut along the fibre radial direction. (a) bar = 1 μm, (b) bar = 500 nm.

system are mostly due to the axial thermal compression and the resulting radial expansions. The theoretical analysis for the aramid fibres suggests increasing radial stresses with increasing curing temperature, however, for the examined curing conditions, the experimental interfacial shear strengths are found to be independent of the curing temperatures. The theoretical interfacial shear stresses are also much greater than the experimental values. These observations suggest that the aramid–epoxy adhesion is substantially limited by a failure process that prevents the interfacial stresses from reaching their theoretical levels.

3.6. Electron microscopy

Direct observation of the fibre–matrix interface is possible through transmission electron microscopy (TEM) of ultra-thin microtomed sections. In the series of micrographs presented here, the direction of the sectioning is indicated by an arrow, fibre and matrix are identified by letters F and M respectively, and the designated magnifications are shown by scale bars.

Figs 10 to 13 illustrate aramid–epoxy composite sections cut along the fibre radius and normal to the fibre long axis. This sectioning direction exerts both tension and compression loads on the fibre–matrix interface. Fig. 10 illustrates the fibrillation that takes place with internal fracture of the fibre and is characteristic of aramid fibre fracture. Similar fibrillation is also seen to occur at the aramid–epoxy interface (Figs 11 to 13). Fig. 11 has isolated a portion of the interface that shows failure to occur with the outer fibre surface or skin. A high magnification of this portion, shows some aramid fibrils pulled away from the fibre, but are still connected to the matrix.

Aramid fibres that have been damaged by the interfacial shear test have been examined (Figs 12 and 13). The cross-section of the axial cracks that are typical of aramid fibre fracture can be seen in Fig. 12. The axial cracks have propagated to the fibre core dividing the fibre into pieces. Another damaged aramid section is shown in Fig. 13. A high magnification observation of the interface documents failure through the fibre surface near the aramid–epoxy interface suggesting good fibre–matrix adhesion, but weak fibre surface properties.

Aramid–epoxy composites have also been sectioned along the other two orthogonal directions. Fig. 14 illustrates the cut along fibre long axis and Fig. 15 shows the cut normal to fibre long axis. Fibre ribbons show repeated bands perpendicular to the cutting direction which are sectioning artifacts. Examination of fibre–matrix interfaces shows both aramid skin failures and interfacial separations. Figs 14a and 15a show examples of internal fibre skin failures. Figs 14b and 15b illustrate fibre–matrix interfacial separations with some fibrils remaining attached to the matrix.

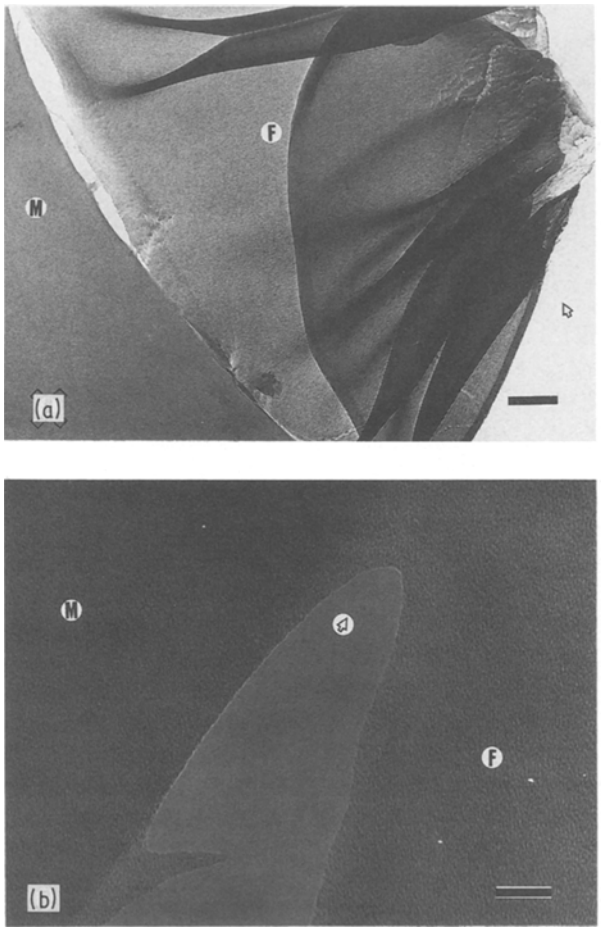

Figure 13 TEM micrographs of a shear damaged Kevlar 49 in a 75° C cured epoxy system. The section is cut along the fibre radial direction. (a) bar = 250 nm, (b) bar = 25 nm.

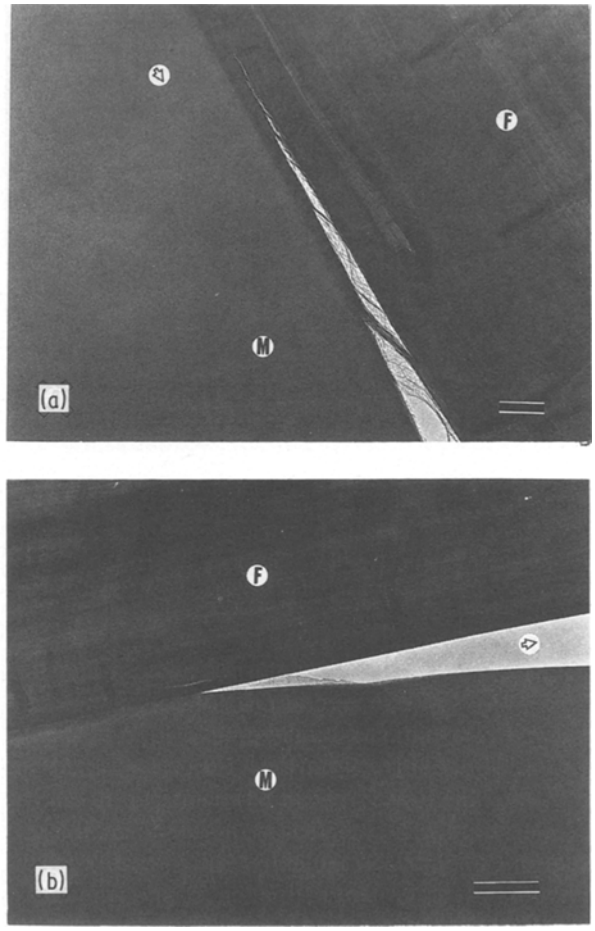

Figure 14 TEM micrographs of Kevlar 49 in a 125° C cured epoxy system. The section is cut along the fibre long axis. (a) bar = 250 nm, (b) bar = 500 nm.

These observations on aramid–epoxy interface suggest that fibre surface layer morphology may be responsible for the low value of fibre–matrix adhesion.

For aramid laminates the fracture surfaces generally show some fibre surface failure in the delamination process [13, 14] confirming the conclusion reached with the single fibre analysis. Fig. 16 illustrates the fracture surface of unidirectional Kevlar 49-epoxy and AS-4-epoxy composites. The composites are made with DER331–MPDA–DETDA system cured at 175° C and have high fibre volume fractions. For the aramid composite extensive fibre surface faillure by fibrillation is evident.

The morphology of the aramid fibres explains the observed mode of interfacial failure. The aramid fibres are composed of large axially oriented polymer macromolecule fibrils that form hydrogen bonds with adjacent molecules [15, 16]. Such a structure will fail by fibrillation. When the applied load is in shear, the fibre exterior must withstand the load and distribute it to the rest of the fibre. For the aramid fibres, it appears that the fibre exterior is incapable of supporting high levels of shear loads without failure within the fibre outer surface layer. Long critical lengths are then required to fully transfer the load across the interface to the fibre.

4. Conclusions

The results of this study lead to following conclusions.

1. Resin shrinkage is not a primary cause of poor adhesion of aramid fibres to epoxy matrices. For the examined curing conditions, the higher thermal stresses at higher curing temperatures did not increase the interfacial shear strength experimentally, reflecting a curing temperature independent failure mechanism.

2. The close matching of aramid radial thermal expansion coefficient and its Poisson ratio to those of the matrix results in low interfacial radial stresses for the aramid fibre–epoxy interface compared to carbon fibre–epoxy interface.

3. High magnification TEM aramid–epoxy interface observations along with fibre coating experiments have shown that the fibre is thermodynamically 'wet' by the matrix.

4. Aramid–epoxy interfacial failure involves failure by fibrillation at the fibre outer surface. This observation suggests the presence of a cohesively weak layer on the fibre exterior that can fail at low shear levels resulting in low values of interfacial shear strength and consequently in insufficient fibre–matrix load transfer.

Acknowledgement

This work was accomplished at the Composite Materials and Structures Center with the cooperation of the Center for Electron Optics of Michigan State University. We wish to gratefully acknowledge E. I. du Pont de Nemours and Company and the State of Michigan Research Excellence Fund for partial financial support for this research.

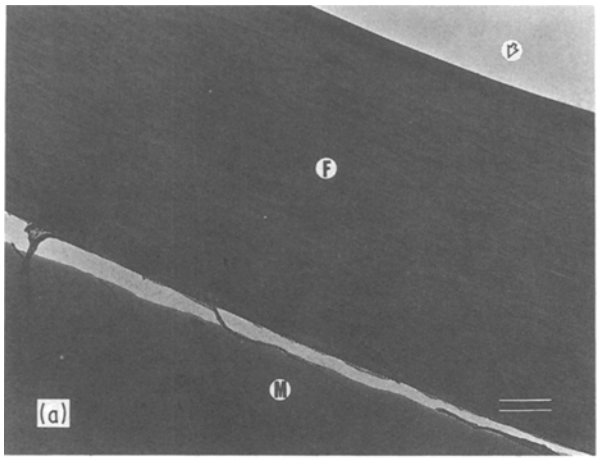

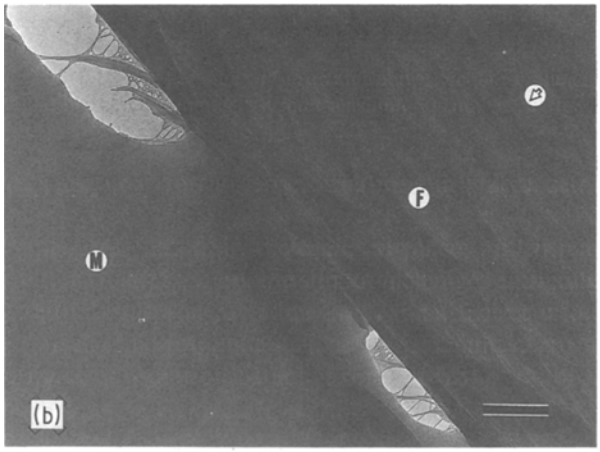

Figure 15 TEM micrographs of Kevlar 49 in a 125° C cured epoxy system. The section is cut normal to the fibre long axis. (a) bar = 1 μm, (b) bar = 500 nm.

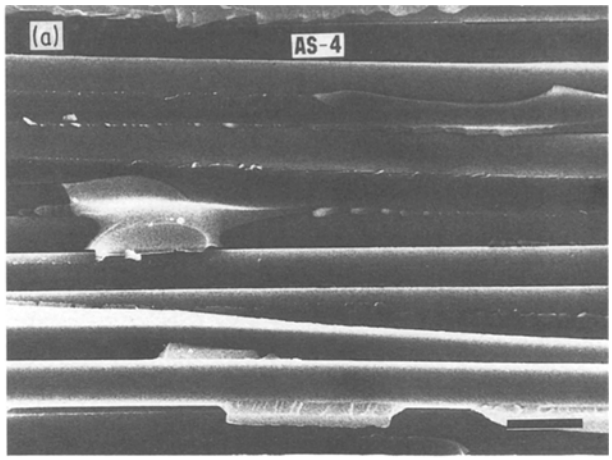

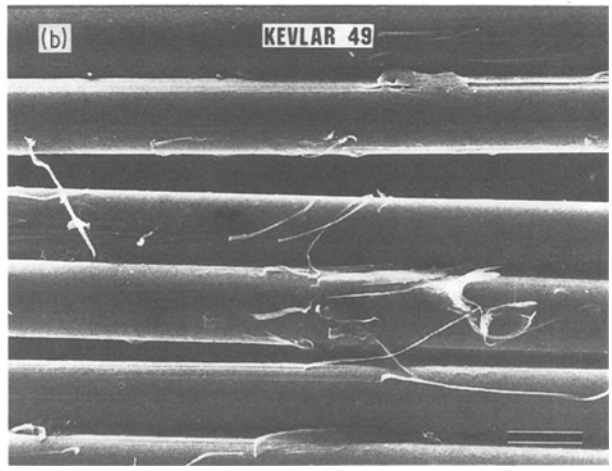

Figure 16 SEM micrographs of fracture surfaces of unidirectional composites. (a) AS-4/epoxy composite. (b) Kevlar 49/epoxy composite. bar = 10 μm.

Appendix

Whitney *et al.* [2], have proposed an approximate solution to the stress distribution around a single fibre fragment using linear elasticity equations. The main assumptions of the Whitney's model are:

(a) the system is axisymmetric,
(b) both fibre and matrix undergo elastic deformations,
(c) fibre is transversely isotropic,
(d) fibre and matrix strains match at their interface, i.e. perfect bonding.

Of particular concern to this study are the shear (τ_{xr}) (MPa) and radial stresses (σ_r) (MPa) involved at the interface. The interfacial shear and the normal stresses are given by the following equations

$$\tau_{xr}(\bar{x}, R) = 4.75\mu A_1 \varepsilon_0 \bar{x} e^{-4.75\bar{x}} \quad \text{(A1)}$$

$$\sigma_r(\bar{x}, R) = [A_2 - \mu^2 A_1(1 - 4.75\bar{x})e^{-4.75\bar{x}}]\varepsilon_0 \quad \text{(A2)}$$

where $\bar{x} = x/l_c$ is a dimensionless length along the fibre axis, ε_0 the far-field axial strain, μ a composite material constant and A_1 and A_2 the elastic constants for axial and radial stress (MPa), respectively. Whitney has described ε_0 as the strain at the onset of observed fibre breakage. Since this parameter is not easily measured, we propose another description

$$\varepsilon_0 = \varepsilon_{uf} - \alpha_m \Delta T \quad \text{(A3)}$$

where ε_{uf} is the fracture strain of the fibre, α_m is the thermal expansion coefficient of the matrix (p.p.m. $°C^{-1}$) and ΔT is the temperature difference (° C) between ambient temperature (25° C) and curing temperature. This description should match the actual strain at the critical length. Other material property constants μ, A_1, A_2, and K_f are defined by

$$\mu = \left(\frac{G_m}{E_{1f} - 4\nu_{12f}G_m}\right)^{1/2} \quad \text{(A4)}$$

$$A_1 = E_{1f}\left(1 - \frac{\bar{\varepsilon}_{1f}}{\varepsilon_0}\right) + \frac{4K_f G_m \nu_{12f}}{K_f + G_m} \times \left(\nu_{12f} - \nu_m + \frac{(1 + \nu_m)\bar{\varepsilon}_m - \bar{\varepsilon}_{2f} - \nu_{12f}\bar{\varepsilon}_{1f}}{\varepsilon_0}\right) \quad \text{(A5)}$$

$$K_f = \frac{E_m}{2\left[2 - \frac{E_{2f}}{2G_{2f}} - \frac{2\nu_{2f}E_{2f}}{E_{1f}}\right]} \quad \text{(A6)}$$

$$A_2 = \frac{2K_f G_m}{K_f + G_m} \times \left(\nu_{12f} - \nu_m + \frac{(1 + \nu_m)\bar{\varepsilon}_m - \bar{\varepsilon}_{2f} - \nu_{12f}\bar{\varepsilon}_{1f}}{\varepsilon_0}\right) \quad \text{(A7)}$$

where K_f is the plane strain bulk modulus (MPa), G_m

is the matrix elastic shear modulus (MPa), G_{2f} the radial fibre elastic shear modulus (MPa) E_m the matrix elastic modulus (MPa), E_{2f} the radial fibre elastic modulus (MPa), ν_{12f} the axial fibre Poisson's ratio, ν_{2f} the radial fibre Poisson's ratio, assumed to be equal to ν_{12f}, ν_m the matrix Poisson's ratio, $\bar{\varepsilon}_m = \alpha_m \Delta T$ the matrix thermal strain, $\bar{\varepsilon}_{1f} = \alpha_{1f} \Delta T$ the axial fibre thermal strain, $\bar{\varepsilon}_{2f} = \alpha_{2f} \Delta T$ the radial fibre thermal strain and α_{1f} and α_{2f} the axial and radial fibre coefficient of thermal expansion (p.p.m. $^\circ C^{-1}$), respectively.

Whitney has defined the critical length (l_c) as the length required to transfer 95% of the applied axial load to the fragment. The definition results in the following equation for the critical length

$$l_c = \frac{2.375R}{\mu} \times 2 \qquad \text{(A8)}$$

which depends explicitly on fibre and matrix material properties, but implicitly on temperature.

Average values of shear and normal stresses are obtained by integrating Equations (A1) and (A2) with respect to $\bar{x}$ and then dividing by the fragment length at $\bar{x} = 1$ to give

$$\bar{\tau}_{theo} \approx 0.200 \mu A_1 \varepsilon_0 \qquad \text{(A9)}$$

$$\bar{\sigma}_{r,theo} \approx (A_2 - 0.00865 \mu^2 A_1) \varepsilon_0 \qquad \text{(A10)}$$

References

1. V. F. ZACKAY, "High-Strength Materials" (John Wiley and Sons, New York, 1964) p. 578.
2. J. M. WHITNEY and L. T. DRZAL, ASTM STP 937 (American Society for Testing and Materials, Philadelphia, 1987) p.179.
3. L. T. DRZAL, M. J. RICH, J. D. CAMPING and W. J. PARK, in Proceedings of the 35th Annual Technical Conference, Reinforced Plastics/Composites Institute, New Orleans, Louisiana 1980 (The Society of the Plastics Industry Inc., 1980) paper 20-C.
4. S. ROJSTACZER, D. COHN and G. MAROM, *J. Mater. Sci. Lett.* **4** (1985) 1233.
5. L. S. PENN, F. A. BYSTRY, W. KARP and S. M. LEE, *Polym. Sci. Technol.* **27** (1985) 93.
6. L. T. DRZAL, in Proceedings of the 15th National SAMPE Technical Conference, Cincinnati, Ohio, October 1983 (SAMPE, Covina California, 1983) p. 190.
7. A. GARTON and J. H. DALY, *Polym. Compos.* **6** (1985) 195.
8. L. T. DRZAL, *J. Adhesion* **16** (1983) 1.
9. T. F. COOKE, *J. Polym. Eng.* **7** (1987) 197.
10. S. K. LI, R. P. SMITH and A. W. NEUMANN, *J. Adhesion* **17** (1984) 105.
11. S. P. WESSON and R. E. ALLRED, in Proceedings of the 7th Annual Meeting of the Adhesion Society, Jacksonville, Florida, 1984 (Adhesion Society, Akron, Ohio, 1984) p. 27.
12. S. J. DeTERESA, R. J. PORTER and R. J. FARRIS, *J. Mater. Sci.* **20** (1985) 1645.
13. H. SAGHIZADEH and C. K. H. DHARAN, *J. Eng. Mater. Technol.* **108** (1986) 290.
14. A. R. BUNSELL, *J. Mater. Sci.* **14** (1975) 1300.
15. M. G. DOBB, D. J. JOHNSON and B. P. SAVILLE, *J. Polym. Sci. Part B* **15** (1977) 2201.
16. R. J. MORGAN, C. O. PRUNEDA and W. J. STEELE, *ibid* **21** (1983) 1757.

Received 9 August
and accepted 8 December 1988